JACS
JOURNAL OF THE AMERICAN CHEMICAL SOCIETY
pubs.acs.org/JACS
Article

Ion Irradiation-Induced Coordinatively Unsaturated Zn Sites for Enhanced CO Hydrogenation

Wei-Peng Shao,◆ Yunjian Ling,◆ Hongru Peng,◆ Jie Luo,◆ Yunjun Cao,◆ Yihua Ran, Jun Cai, Jiayu Lv, Bowen Zhu, Yun Liu, Yuxiang Chen, Na Li, Feng Jiao, Huiqi Chen, Yifeng Zhu, Xin Ou, Yuemin Wang, Christof Wöll, Qiang Fu, Xiulian Pan, Peijun Hu, Wei-Xue Li,* Zhi Liu,* Xinhe Bao, and Fan Yang*

Cite This: https://doi.org/10.1021/jacs.4c13234

Read Online

ACCESS | Metrics & More | Article Recommendations | Supporting Information

ABSTRACT: Defect engineering critically influences metal oxide catalysis, yet controlling coordinatively unsaturated metal sites remains challenging due to their inherent instability under reaction conditions. Here, we demonstrate that high-flux argon ion (Ar^+) irradiation above recrystallization temperatures generated well-defined coordinatively unsaturated Zn (CUZ) sites on ZnO($10\bar{1}0$) surfaces that exhibited enhanced stability and activity for CO hydrogenation. Combining low-temperature scanning probe microscopy, ambient pressure X-ray photoelectron spectroscopy, and surface−ligand infrared spectroscopy with density functional theory calculations, we identified <$1\bar{2}10$> step edges exposing CUZ sites as the dominant active sites. These sites facilitate hydrogen-assisted CO dissociation through a mechanism distinct from formate-mediated pathways on stoichiometric ZnO. The ion-irradiation approach effectively addressed instability of Zn species, a major problem in ZnO catalysis, enabling stable performance in syngas conversion when combined with zeolites. Our atomic scale investigation provided spectroscopic fingerprints for active sites on the ZnO catalyst and insights into the structure−activity relationships of ZnO for CO hydrogenation. Our approach for engineering thermally stable defect sites in oxide catalysts provided opportunities for rational catalyst design beyond traditional preparation methods.

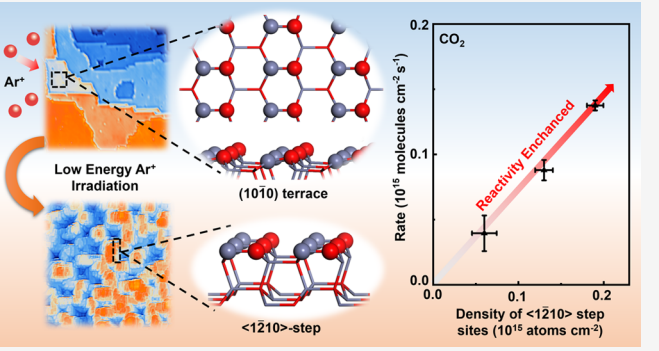

INTRODUCTION

Metal oxides undergo defect engineering to optimize their properties for technological applications, such as electronics, optoelectronics, sensors, and catalysis. In particular, surface defects play a crucial role in determining the chemical properties of metal oxides.[1−4] In catalysis, understanding and controlling surface defects is essential for tailoring the catalytic properties of metal oxides,[5−8] although these defect structures remain mostly unresolved. Coordinatively unsaturated metal (CUS) centers[3] have been proposed as active sites on metal oxide catalysts. Their dispersion and stability could be tuned by varying the size,[9] shape,[10,11] and oxidation state[8,12] of oxide nanocatalysts. However, resolving the atomic structures of CUS sites on oxide nanocatalysts remains challenging. Despite studies of CUS sites on single-crystal oxide surfaces,[13−15] the "materials gap" complicates applying insights from planar oxides to practical catalysts with varied CUS site coordination environments.

Here, we combine model and powder catalytic studies to elucidate the structure−activity relationship of ZnO for CO hydrogenation. Defects on nanoscale ZnO critically influence its properties like p-type conductivity[16,17] and hydrogenation catalysis.[18,19] With a growing focus on sustainable energy, C1 chemistry, particularly CO_x (CO and CO_2) hydrogenation, shows promise for valuable chemical production. Among CO_x hydrogenation catalysts, ZnO-based materials have demonstrated exceptional performance.[5,20−22] The catalytic activity of ZnO arises from its ability to dissociate H_2 and activate CO_x molecules,[5,22] although the reaction mechanism of CO hydrogenation has remained elusive.[23] When combined with zeolites as bifunctional oxide-zeolite (OXZEO) composites, these catalysts showed synergistic enhancements in syngas conversion.[5,19,21]

The performance of ZnO primarily depends on surface defects, specifically coordinatively unsaturated Zn (CUZ) sites,[9,19] rather than point defects.[24] Understanding the

Received: September 22, 2024
Revised: January 15, 2025
Accepted: January 16, 2025

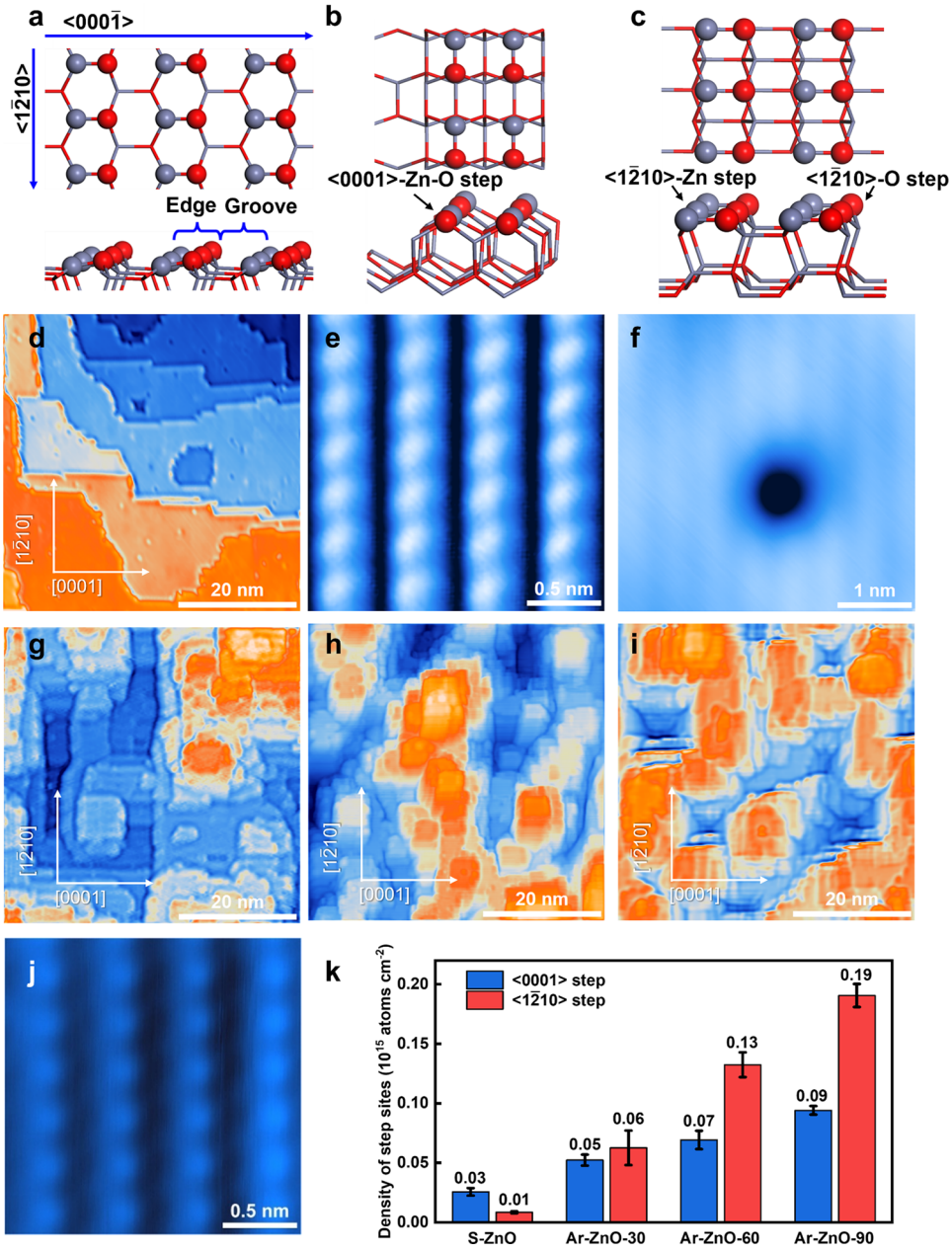

Figure 1. Surface structures of stoichiometric ZnO(10$\bar{1}$0) (S-ZnO) and Ar^+-irradiated ZnO(10$\bar{1}$0) (Ar-ZnO). (a−c) Structural models of the terrace, <0001> and <1$\bar{2}$10> steps of ZnO(10$\bar{1}$0). (d) Large-scale and (e, f) atomic resolution STM images of S-ZnO. A typical defect structure on S-ZnO is displayed in (f). STM images of ZnO(10$\bar{1}$0) irradiated by high-flux Ar^+ beam for (g) 30 min (Ar-ZnO-30), (h) 60 min (Ar-ZnO-60), and (i) 90 min (Ar-ZnO-90), respectively. (j) Constant height nc-AFM image showing the atomic resolution of the Ar-ZnO surface at a tip height of −400 pm. The tip height was referenced to the STM set point (V_s = 2.0 V, I_t = 0.1 nA). (k) Surface density of step sites along <0001> or <1$\bar{2}$10> steps on S-ZnO and Ar-ZnO surfaces. Scanning parameters: (e) V_s = 0.66 V, I_t = 0.5 nA; (f) V_s = 1.0 V, I_t = 0.5 nA.

structural nature and distribution of these defects holds broad significance. A significant challenge lies in the stability of defect sites within Zn-based oxides. Under reducing conditions and elevated temperatures, surface defects, particularly low-coordination Zn sites, are prone to migration and volatilization under reducing conditions.[25−28] During CO hydrogenation, Zn species could migrate to neighboring zeolites, affecting catalytic properties.[19,29] For instance, the migration of Zn onto SAPO-34 was found to form Zn-OH on Brønsted acid sites, reducing light olefin selectivity through increased hydrogenation.[29] Mobile Zn ions could neutralize protons on H-ZSM-5 through solid-state ion exchange, leading to catalyst deactivation.[25] Active Zn species suffered from Zn reduction and volatilization, as further manifested by the $ZnZrO_x$ catalyst in CO_2 hydrogenation[30] and ZnO_x in propane dehydrogenation (PDH) reaction.[31] To improve ZnO_x stability, researchers have modified ZnO with Pt to enhance Lewis acidity[32] or combined ZnO with zeolites or other oxides.[27] These studies demonstrate that preventing Zn reduction and volatilization is essential for maintaining the catalyst performance.

The instability of defect sites in ZnO could stem from insufficient crystallization. Although high-temperature crystallization could improve stability, it also reduces the number of active sites.[9] Hereby, we introduce an ion irradiation strategy utilizing high-flux argon ions (Ar^+) to produce well-defined

https://doi.org/10.1021/jacs.4c13234
J. Am. Chem. Soc. XXXX, XXX, XXX−XXX

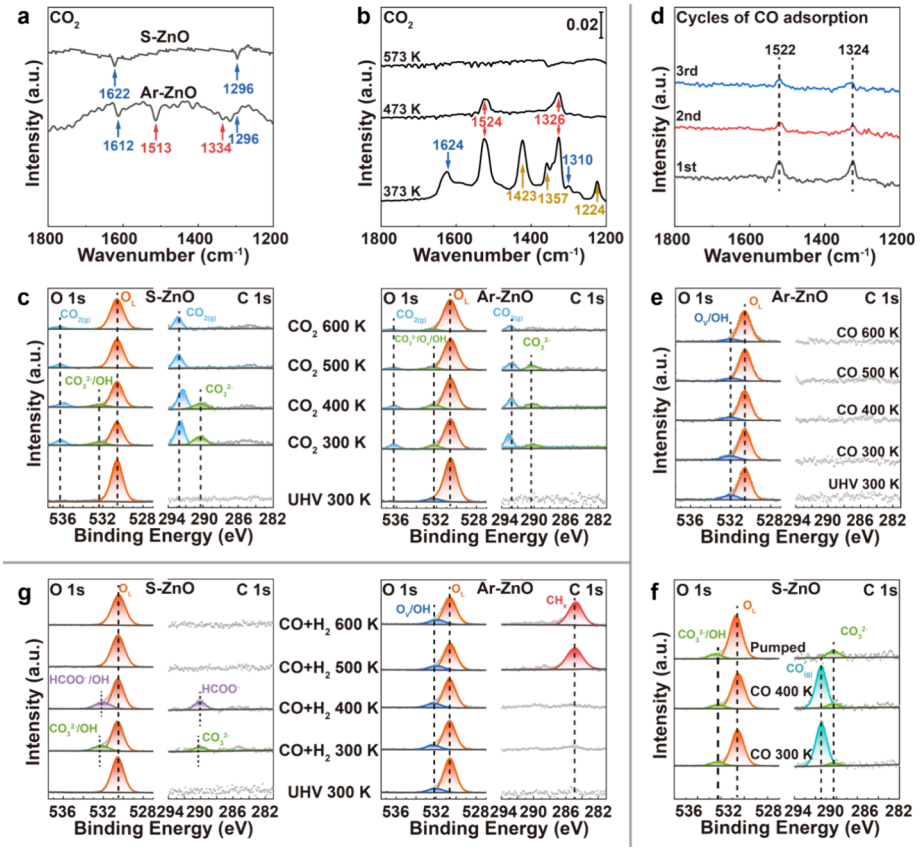

Figure 2. Interaction of CO and CO_2 with S-ZnO, Ar-ZnO and powder ZnO catalysts. (a) IRRAS spectra of S-ZnO and Ar-ZnO-60 exposed to CO_2. (b) DRIFTS spectra of powder ZnO exposed to CO_2 flow (10 mL/min, 5% CO_2/Ar). (c) AP-XPS O 1s and C 1s spectra of S-ZnO and Ar-ZnO-60 surfaces exposed to 1 mbar CO_2 at elevated temperatures. (d) DRIFTS spectra of powder ZnO upon cycles of CO exposure (373 K, 10 mL/min, 5% CO/Ar) and CO desorption (473 K, 10 mL/min, Ar). (e, f) AP-XPS O 1s and C 1s spectra of Ar-ZnO-60 and S-ZnO surfaces upon exposure to 0.15 mbar CO at elevated temperatures. (g) AP-XPS O 1s and C 1s spectra of S-ZnO and Ar-ZnO-60 surfaces upon exposure to 0.6 mbar CO/H_2 mixture gas (CO:H_2 = 1:3) at elevated temperatures.

CUZ sites that maintain both activity and stability during CO hydrogenation. Ion irradiation is a versatile material processing technique that can be readily scaled up for industrial applications. The technique has been generally employed to introduce controlled defects into oxides and semiconductors[33−35] and has been established as a controllable method for defect engineering and surface nanopatterning.[36−38] We irradiated the ZnO($10\bar{1}0$) surfaces by Ar^+ at 750 K (Ar-ZnO), which were then investigated combining low-temperature scanning tunneling microscopy (LT-STM), ambient pressure X-ray photoelectron spectroscopy (AP-XPS), surface-ligand infrared (SLIR) spectroscopy,[39] synchrotron vacuum ultraviolet photoionization mass spectrometry (SVUV-PIMS), density functional theory (DFT) calculations, and model catalytic studies. Our results demonstrate that Ar-ZnO surfaces effectively model the structural and reaction properties of practical ZnO catalysts for CO hydrogenation, providing spectral fingerprints for active sites on ZnO and enabling atomic scale investigation of structures−activity relationships. The study also provided a scalable method to enhance both the activity and selectivity of the ZnO catalyst for syngas conversion, marking a significant advance in the field of metal oxide catalysis.

RESULTS AND DISCUSSION

Structures of Stoichiometric and Defective ZnO Model Catalysts. ZnO($10\bar{1}0$), as the most stable surface of ZnO,[40] exhibits 3-fold coordinated Zn (Zn_{3c}) and O (O_{3c}) atoms at both terrace and step sites (Figure 1a). The surface features three distinct step configurations: a mixed Zn-O termination along the <0001> direction (<0001>-Zn-O, Figure 1b), and Zn termination (<$1\bar{2}10$>-Zn), or O termination along the <$1\bar{2}10$> direction (<$1\bar{2}10$>-O, Figure 1c). STM of the pristine ZnO($10\bar{1}0$) surface exhibited flat terraces with a rectangular unit cell oriented along the <0001> and <$1\bar{2}10$> directions (Figure 1d), having lattice constants of 0.53 and 0.33 nm, respectively (Figure 1e). The bright rows in STM images (Figure 1e,f), acquired under positive sample bias, correspond to the topmost Zn rows along the <$1\bar{2}10$> direction, since the Zn 4s states contribute to the conduction band minimum of ZnO.[41,42] Surface defects on ZnO($10\bar{1}0$) appeared as dark spots within the bright Zn rows (Figure 1f) and were identified as Zn−O dimer vacancies,[43] with a concentration of less than 1%. Thus, the pristine ZnO($10\bar{1}0$) surface could be considered stoichiometric (denoted as S-ZnO), with CUZ sites predominantly located at step edges.

To engineer defective ZnO surfaces with CUZ sites, Zn atoms were initially evaporated onto ZnO($10\bar{1}0$) to form supported ZnO_x clusters, as confirmed by XPS analysis.[43] However, these supported ZnO_x clusters exhibited poor thermal stability, decomposing and evaporating at above 450 K under a CO atmosphere, which resulted in the recovery of the ZnO surface to its stoichiometric state, as evidenced by AP-XPS (Figure S1). Therefore, engineering the oxide

https://doi.org/10.1021/jacs.4c13234
J. Am. Chem. Soc. XXXX, XXX, XXX−XXX

substrate to stabilize CUZ sites is essential for enhancing the catalytic performance of ZnO-based catalysts.

We then implement high-flux Ar^+ irradiation to modify ZnO($10\bar{1}0$) at temperatures exceeding the recrystallization threshold of ZnO. The process operates by irradiating materials with gas ions, which cause cascading collisions, thereby introducing defects in a controlled manner and enabling subsequent adjustment of physical and chemical properties.[44,45] At elevated temperatures, ion-induced interstitials and vacancies exhibit sufficient mobility to either recombine or migrate to the surface before subsequent ion impacts occur in the same region. Consequently, ion irradiation performed above the recrystallization temperature prevents amorphization while stabilizing surface vacancies since their diffusion and annihilation are inhibited by the Ehrlich−Schwoebel (ES) barrier.[46]

Three ZnO($10\bar{1}0$) surfaces were subjected to Ar^+ irradiation at 750 K for 30, 60, and 90 min, respectively, and were designated as Ar-ZnO-30, Ar-ZnO-60, and Ar-ZnO-90. STM analysis revealed significant morphological changes characterized by increased step density correlating with irradiation duration. The average topmost terrace size decreased to ∼5 nm (Figures 1g−i and S2b−d). The irradiation process generated surface vacancies and initiated depression nucleation on ZnO($10\bar{1}0$), leading to a distinct self-organized three-dimensional (3D) morphology through coarsening. Notably, the fundamental terrace structure remained intact postirradiation (Figure S3), with lattice parameters showing no measurable differences between Ar-ZnO and S-ZnO surfaces (Figure 1j). The highly corrugated morphology of Ar-ZnO surfaces caused difficulties for atomic resolution imaging with close tip−surface proximity (Figure S3). Noncontact atomic force microscopy (nc-AFM) was thus used to enable a closer tip−surface distance and resolve the atomic lattice of Ar-ZnO (Figure 1j). STM analysis also identified point defects on the Ar-ZnO surface terraces, though at minimal concentrations below 1%. However, the distribution of step sites changed significantly.

The S-ZnO surface predominantly featured <0001> step sites, characterized by alternating Zn_{3c} and O_{3c} atoms. Following Ar^+ irradiation, the density of <$1\bar{2}10$> step sites on Ar-ZnO increased substantially (Figures 1k and S2e). An analysis of step site densities (detailed in SI, Figures S4 and S5) demonstrated a drastic increase by more than an order of magnitude, in the density of <$1\bar{2}10$> step sites after irradiation. Meanwhile, <0001> step sites showed only modest density increases. This process effectively reversed the dominant step structure distribution compared to preirradiation conditions. The experimental protocol employed Ar^+ specifically for surface nanopatterning, chosen for its chemical inertness. This selection proved effective, as validated by measurements of valence band spectra showing negligible changes in electronic structure before and after irradiation (Figure S6).

The formation of step CUZ sites on the Ar-ZnO surfaces was further corroborated by XPS. A notable deviation from the symmetric O 1s peak characteristic of S-ZnO was observed in the O 1s spectra of Ar-ZnO, which exhibited a shoulder peak at 531.9 eV that remained stable at elevated temperatures (Figure S7). Since hydroxyls and carbonates decompose and desorb below 600 K, we could attribute the 531.9 eV peak to oxygen anions (O_v) adjacent to CUZ sites, whose intensity correlated with the duration of Ar^+ irradiation (Figure S8). Furthermore, STM showed minimal terrace defects on both the S-ZnO and Ar-ZnO surfaces, confirming that the O_v peak is likely associated with step sites rather than terrace sites.

Correlating Adsorption and Reaction Properties of S-ZnO and Ar-ZnO with Powder ZnO. The adsorption properties of S-ZnO and Ar-ZnO were first examined by infrared reflection absorption spectroscopy (IRRAS) using CO_2 as a probe molecule (Figure 2a). While CO_2 chemisorbed on terrace sites of S-ZnO as tridentate carbonate,[47] as evidenced by peaks at 1622 and 1296 cm^{-1}, IR spectrum of CO_2 adsorption on Ar-ZnO showed additional peaks at 1513 and 1334 cm^{-1}, indicative of bidentate carbonate at step sites. For comparison, powder ZnO catalysts were synthesized by a coprecipitation method and exhibited the same hexagonal wurtzite phase[9] (detailed in SI, Figure S9). Diffuse reflectance infrared Fourier transform spectroscopy (DRIFTS) of CO_2 adsorption on powder ZnO showed the emergence of peaks at 1624/1310, 1524/1326, and 1423/1357/1224 cm^{-1} (Figure 2b), which could be assigned to carbonates adsorbed at terrace, step, and surface defect sites.[48,49] Monodentate carbonates adsorbed at surface defect sites exhibited limited thermal stability, desorbing upon heating to 473 K (Figure 2b). In contrast, step site carbonates demonstrated enhanced stability at elevated temperatures, suggesting stronger binding interactions.

AP-XPS studies confirmed carbonate formation on both S-ZnO and Ar-ZnO surfaces (Figure 2c), with Ar-ZnO showing superior thermal stability. Carbonates on Ar-ZnO persisted above 500 K, while those on S-ZnO desorbed completely by 500 K. Previous studies[50,51] suggested that CO_2 adopts a tridentate configuration on ZnO($10\bar{1}0$), forming bonds between carbon atoms and 3-fold coordinated O (O_{3c}) sites, while oxygen atoms interact with adjacent 3-fold coordinated Zn (Zn_{3c}) sites along the <0001> direction. Our DFT calculations showed significant differences in CO_2 adsorption energies between <$1\bar{2}10$> step and ($10\bar{1}0$) terrace sites, respectively (−6.34 and −5.99 eV, Figure S10). This energetic difference explains the enhanced thermal stability of carbonates at step sites on Ar-ZnO compared to terrace sites on S-ZnO. Temperature-programmed AP-XPS experiments demonstrated complete carbonate desorption below 600 K, consistent with observations from powder ZnO catalysts studies.

DRIFTS studies of powder ZnO under CO exposure further confirmed the assignment of step carbonates, showing peaks at 1522 and 1324 cm^{-1} (Figures 2d and S11).[48,52] We have previously demonstrated that CO selectively reacts with lattice oxygen at step sites, rather than at terrace or terrace defect sites.[24,53] The observed decrease in the intensities of the 1522/1324 cm^{-1} peaks during successive CO adsorption−desorption cycles (Figure 2d) indicated the removal of lattice oxygen from the step sites via CO_2 desorption, generating oxygen-deficient step sites. The extent of carbonate formation served as an indicator of ZnO surface reduction. Comparative AP-XPS studies of CO reactions on Ar-ZnO and S-ZnO showed distinct behaviors. While no carbonate formation was obvious on Ar-ZnO (Figure 2e), S-ZnO in 0.15 mbar CO exhibited carbonate formation between 300 and 400 K (Figure 2f). These spectroscopic results confirmed the similarity between CUZ sites on Ar-ZnO and defect sites on powder ZnO, demonstrating comparable adsorption and reaction properties toward CO and CO_2. Using CO and CO_2 as probe molecules, Ar-ZnO provided reference spectra for SLIR[39] of powder ZnO and could serve as a model system for ZnO catalysts under reducing conditions.

https://doi.org/10.1021/jacs.4c13234
J. Am. Chem. Soc. XXXX, XXX, XXX−XXX

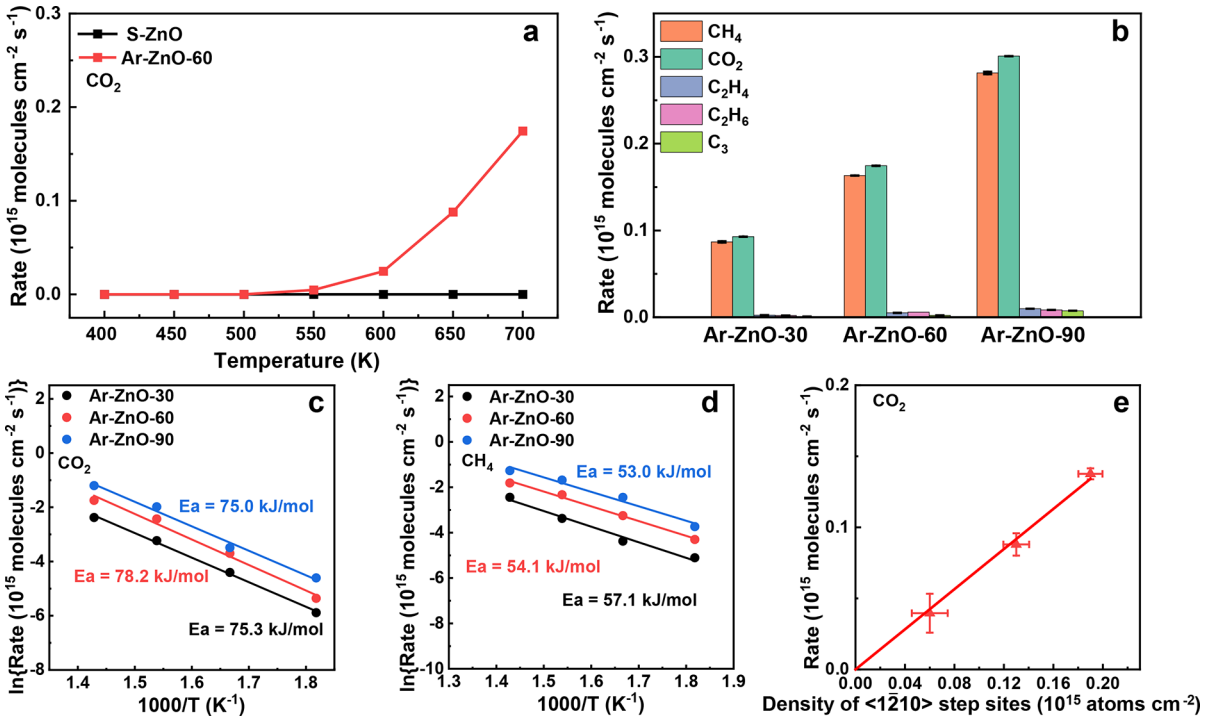

Figure 3. Reaction kinetics of S-ZnO and Ar-ZnO in CO hydrogenation and their correlation with surface defect sites. (a) Comparison of CO_2 formation rates during CO hydrogenation on S-ZnO and Ar-ZnO-60. (b) Formation rates of gas phase products, measured by online GC, in CO hydrogenation ($CO:H_2$ = 1:3, 10 mL/min) at 700 K on Ar-ZnO-30, Ar-ZnO-60, and Ar-ZnO-90. Arrhenius plots are displayed for (c) CO_2 and (d) CH_4 production during CO hydrogenation. (e) Plot of CO_2 formation rate at 650 K as a function of surface density of <1$\bar{2}$10> step sites.

Subsequently, CO hydrogenation was studied using AP-XPS, showing the formation of formate species on S-ZnO at 400 K (Figure 2g). No formate was observed on Ar-ZnO in the CO/H_2 mixture gas. Rather, atomic carbon or hydrocarbon species emerged on Ar-ZnO at 500 K (Figure 2g), indicating the occurrence of CO dissociation. Despite the increased step density on Ar-ZnO, its interaction with CO remained weak, with CO adsorption only observed under cryogenic conditions (Figure S12). The Ar-ZnO surface remained intact even in 0.15 mbar CO (Figure 2e). Thus, CO dissociation on Ar-ZnO likely proceeds via a hydrogen-assisted CO disproportionation process to form CH_x species ($CO^* + H^* \rightarrow CHO^*$; $CHO^* \rightarrow CH^* + O^*$) and CO_2 ($CO + O^* \rightarrow CO_2$), with the former hydrogenated to CH_4 at higher temperatures. The observed correlation between the diminution of surface CH_x species and the substantial formation of CH_4 corroborates their transformation. This mechanism aligns with previous mechanistic studies by Lai et al.,[54] showing preferential pathways via *CHO intermediates, which can dissociate to form CH_4 and CH_2CO.

Reaction studies of S-ZnO and Ar-ZnO in CO hydrogenation provided further evidence for CUZ sites as active centers and supported the proposed mechanism involving hydrogen-assisted CO dissociation, followed by hydrogenation steps. When exposed to a CO/H_2 mixture gas, S-ZnO exhibited negligible reactivity up to 700 K (Figure 3a), corroborated by AP-XPS C 1s spectra indicating the absence of CH_x formation during CO hydrogenation (Figure 2g). In contrast, Ar-ZnO exposed to the CO/H_2 mixture showed the production of CO_2 and CH_4 (Figure 3b), along with minor products including C_2H_4, C_2H_6, and C_3 hydrocarbons, as detected by online gas chromatography (GC). The unity ratio between produced hydrocarbon and CO_2 at 700 K supported the proposed mechanism.

The reaction properties of reduced powder ZnO were found similar to that of Ar-ZnO in CO hydrogenation. DRIFTS conducted at 623 K showed no formate species on the reduced powder ZnO (Figure S13). Continued H_2 treatment at elevated temperatures after CO/H_2 activation over powder ZnO catalysts yielded small production of CH_4, alongside minimal C_2H_2 and C_2H_4 signals and C_3H_5 fragments, as detected by SVUV-PIMS, indicating hydrocarbon deposition prior to hydrogenation (Figure S14). In contrast, no methoxy (CH_3O) or dimethyl ether (CH_3OCH_3) was detected. Thus, upon reduction of powder ZnO, hydrogen-assisted CO disproportionation likely occurred during syngas conversion above 600 K. Our findings suggest that the formation of formate species requires available lattice oxygen with the reaction pathway shifting to CO disproportionation upon further reduction of ZnO.

Identifying the Structure of Active Sites on ZnO for CO Hydrogenation. Reaction kinetics of CO hydrogenation over S-ZnO and Ar-ZnO catalysts provided crucial insights into active site identification and structure−activity relationships. While S-ZnO exhibited negligible activity, the catalytic performance measured over a series of Ar-ZnO catalysts demonstrated remarkable consistency among these model catalysts. CO_2 generation between 550 and 700 K exhibited similar apparent activation energies of 75.3, 78.2, and 75.0 kJ/mol for Ar-ZnO-30, Ar-ZnO-60, and Ar-ZnO-90, respectively (Figure 3c). Likewise, CH_4 production displayed comparable apparent activation energies ranging from 57.1 kJ/mol for Ar-ZnO-30, 54.1 kJ/mol for Ar-ZnO-60, to 53.0 kJ/mol for Ar-ZnO-90 (Figure 3d). The higher activation energy for CO_2 formation indicated that hydrogen-facilitated CO dissociation,

https://doi.org/10.1021/jacs.4c13234
J. Am. Chem. Soc. XXXX, XXX, XXX−XXX

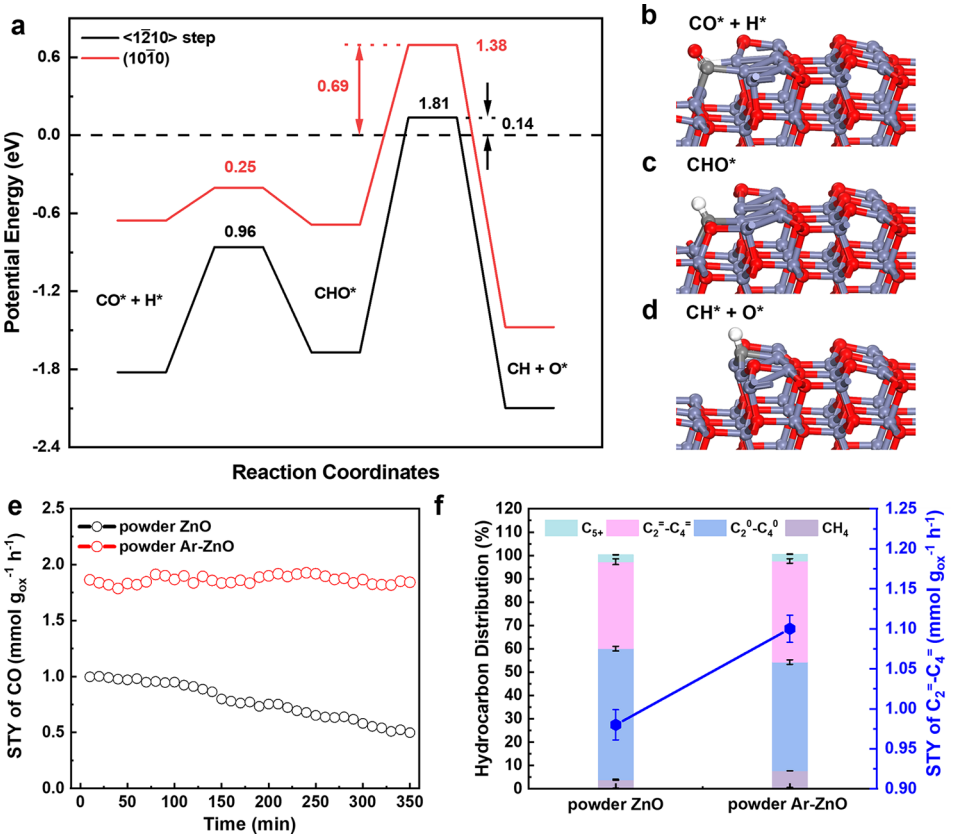

Figure 4. DFT calculations of hydrogen-assisted CO dissociation at the <1$\bar{2}$10> step on Ar-ZnO and optimization of powder ZnO catalysts. (a) Calculated potential energies showing hydrogen-assisted CO dissociation at the <1$\bar{2}$10> step (black line) over CO desorption on the (10$\bar{1}$0) terrace (red line). Reference point for the potential energy surface is defined as the energy of gaseous CO and H_2, along with the surface containing oxygen vacancies. (b–d) Optimized structures of reaction intermediates of CO dissociation at the <1$\bar{2}$10> step. Optimized structures of reaction intermediates of CO dissociation at the (10$\bar{1}$0) terrace are shown in Figure S18. Gray, red, and brown spheres represent Zn, O, and C atoms, respectively. (e) Reaction rates of CO hydrogenation as a function of time over powder ZnO and powder Ar-ZnO catalysts. Space time yield (STY) was calculated from CO conversion at 673 K. Reaction conditions: CO:H_2 = 1:2.5, 673 K, 0.1 MPa, and gas hourly space velocity (GHSV) = 4800 mL·h^{-1}·g_{ox}^{-1}. (f) Catalytic performance of syngas conversion over OXZEO composites by mixing powder ZnO or powder Ar-ZnO catalysts with SAPO-34. Hydrocarbon distribution and STY toward light olefins ($C_2^=$–$C_4^=$) are compared. Reaction conditions: CO:H_2 = 1:2.5, 673 K, 4.0 MPa, and GHSV = 4800 mL·h^{-1}·g_{ox}^{-1}.

rather than CH_x hydrogenation, constituted the rate-determining step. The consistency across different Ar-ZnO catalysts suggested identical active sites, which could be further identified by correlating the CO_2 formation rate with the density of each site type on the series of model catalysts.

Spectroscopic quantification of active sites presents significant challenges in distinguishing different types of CUZ sites. To address previous limitations in oxygen vacancy (O_v) characterization,[55] O 1s spectra were acquired under ultrahigh vacuum (UHV) conditions at 600 K, ensuring complete desorption of surface OH species.[56] Unlike earlier theoretical studies[55,57] focusing on terrace point defects, our investigation examined step edge defects generated through Ar^+ irradiation, which exhibited distinct spectroscopic signatures in O 1s spectra. Recognizing that O 1s spectra alone provide insufficient evidence, we corroborated O 1s spectra with changes in metal oxidation states, which are evident in the Zn 3d spectra (Figure S15a).[58] Although a linear correlation between the CO_2 formation rate and the $Zn^{\delta+}/Zn^{2+}$ ratio could be observed (Figure S15b), the plot did not intersect with the zero point. Nonetheless, AP-XPS Zn 3d spectra could be used to monitor the dynamic stability of CUZ sites on Ar-ZnO catalysts during CO hydrogenation. The peak intensities corresponding to $Zn^{\delta+}$ at 9.9 eV in the Zn 3d spectra were found consistent during CO hydrogenation at elevated temperatures (Figure S16) and the catalytic reactivity remained stable (Figure S17), indicating that CUZ sites engineered by Ar^+ irradiation are stable for CO hydrogenation.

The structure–activity relationship for Ar-ZnO model catalysts could be further established from STM analysis, which showed two types of step site structures on ZnO(10$\bar{1}$0). Comparison of S-ZnO and Ar-ZnO-30 surfaces showed significantly higher density of <1$\bar{2}$10> step sites on Ar-ZnO-30, while the density of <0001> step sites was only marginally higher (Figure 1k). This suggests that <1$\bar{2}$10> step sites, which exhibited the greatest density variation with irradiation time, likely serve as active sites for CO hydrogenation. Indeed, a direct linear correlation, intersecting the zero point, could be observed between CO_2 formation rates and the densities of <1$\bar{2}$10> step sites (Figure 3e). In contrast, the correlation between CO_2 formation rates and <0001> step site densities did not intersect the zero point (Figure S15c).

The active site structure was corroborated by the DFT calculations. We have shown that terrace sites of ZnO(10$\bar{1}$0) are inactive for CO dissociation but facilitate CO hydrogenation to formate species.[24] In contrast, <1$\bar{2}$10> step sites exhibit significantly enhanced reactivity for CO dissociation (Figure 4a). While the binding of CO at step sites of Ar-ZnO

https://doi.org/10.1021/jacs.4c13234
J. Am. Chem. Soc. XXXX, XXX, XXX–XXX

was slightly stronger at Zn_{2c} sites, DFT calculations suggested that a minimum of two adjacent oxygen vacancies were required for effective CO dissociation (Figure 4b–d). DFT results indicated that reduced O-terminated <1$\bar{2}$10> step sites exhibit the highest CO dissociation activity, owing to their abundance of CUZ sites, making them the most active sites for hydrogen-assisted CO dissociation. Figure 4a showed that the <1$\bar{2}$10> step edges enhance the adsorption of CO and H_2 when compared to the (10$\bar{1}$0) terraces. The two adjacent oxygen vacancies on (10$\bar{1}$0) terraces show low reactivity (Figure S18). Although the activation energy barriers for the elementary reactions of CO hydrogenation and CHO* bond dissociation at the reduced <1$\bar{2}$10> step are higher compared to the (10$\bar{1}$0) surface, the apparent activation barrier relative to the reaction starting point decreases from 0.69 to 0.14 eV. Additionally, the reduced step edges enhance the adsorption of the produced CH* and O*, making the reaction thermodynamically more favorable. Therefore, the partially reduced step edges with their abundance of CUZ sites were the most active for hydrogen-assisted CO dissociation. The reduction of O-terminated <1$\bar{2}$10> step sites has been observed after exposure to 0.5 mbar CO at 400 K (Figure S19). STM images indicated missing rows along the <1$\bar{2}$10> direction, suggesting the formation of oxygen vacancy chains.

Previous studies[59−61] on CO_2 hydrogenation over ZnO have emphasized the structure-sensitive nature of ZnO for methanol synthesis, with highly crystalline surfaces showing superior performance compared to higher surface area and lower crystallinity ZnO nanomaterials.[60] Kurtz et al.[59] studied methanol synthesis from CO/CO_2 hydrogenation over ZnO and suggested that CO_2 acts as a catalyst poison for ZnO catalysts by oxidizing active sites, which highlights the importance of maintaining oxygen vacancies for optimal catalytic performance. The primary reaction pathway was found to involve CO hydrogenation. These findings suggest potential applications for Ar-ZnO as model catalysts in studies of methanol synthesis, particularly on polar ZnO surfaces.

Optimization of Powder ZnO Catalysts for CO Hydrogenation. The inherent instability of low-coordination Zn sites in powder ZnO presents a significant challenge for catalytic applications. While previous study[9] has shown that high-temperature calcination could enhance defect site stability, this approach substantially reduced the density of active sites due to increased particle size. Here, our Ar^+ irradiation approach could effectively address this limitation by simultaneously improving the defect site stability and eliminating Zn sites susceptible to reduction and volatilization. High-flux Ar^+ irradiation was employed to engineer dynamically stable CUZ sites on powder ZnO catalysts (denoted as powder Ar-ZnO). While XPS Zn 2p and Zn LMM spectra showed no detectable differences between powder ZnO and powder Ar-ZnO (Figure S20a,b), XPS Zn 3d spectra of powder Ar-ZnO exhibited a slight shift toward lower binding energy compared to powder ZnO (Figure S20c). Peak deconvolution of Zn 3d spectra showed an increase in the intensity ratio of $Zn^{\delta+}/Zn^{2+}$ from 31.8% to 48.3% for powder Ar-ZnO (Figure S20c,d), indicating surface enrichment of stable CUZ sites.

Catalytic activities of powder ZnO and powder Ar-ZnO were evaluated through CO hydrogenation reactions. Under atmospheric pressure conditions (Figure 4e), the space time yields of CO conversion increased from 1.0 $mmol \cdot g_{ox}^{-1} \cdot h^{-1}$ for powder ZnO to 1.8 $mmol \cdot g_{ox}^{-1} \cdot h^{-1}$ for powder Ar-ZnO. These results demonstrate that high-flux Ar^+ irradiation effectively increased CUZ sites on powder ZnO, thereby enhancing its catalytic activity for CO hydrogenation. Furthermore, powder Ar-ZnO exhibited superior catalytic stability compared to powder ZnO (Figure 4e), suggesting that the active CUZ sites formed by high-flux and high-temperature Ar^+ irradiation are more stable and resistant to volatilization.

The enhanced stability of powder Ar-ZnO proved to be particularly valuable when combined with zeolite catalysts. Previous studies[25,26,29] have indicated that migration of Zn species to zeolites under harsh reaction conditions affects the production and distribution of hydrocarbons, particularly the selectivity toward light olefins. However, when physically mixed with SAPO-34 and tested for syngas conversion at 673 K and 4.0 MPa, powder Ar-ZnO maintained stable catalytic activity (Figure S21), contrasting with previously reported deactivation behaviors due to ZnO volatilization/migration.[25,29] This stability demonstrates the effective preservation of surface defects during both mixing and catalysis processes. Compared to powder ZnO, powder Ar-ZnO demonstrated higher space time yields and enhanced selectivity toward light olefins (Figure 4f). Our findings suggest high-temperature Ar^+ irradiation as a promising strategy for enhancing powder ZnO catalysts, offering simultaneous improvements in activity, stability, and selectivity for syngas conversion.

CONCLUSIONS

Our Ar^+ irradiation strategy generated well-defined and stable CUZ sites on ZnO catalyst surfaces, enhancing their catalytic performance in CO hydrogenation. A comprehensive analysis of the active site structure and reaction properties of both model and powder ZnO catalysts was achieved through combined studies using LT-STM, SLIR, AP-XPS, SVUV-PIMS, and DFT calculations and catalytic tests. Our results identified CUZ sites at the <1$\bar{2}$10> steps of Ar-ZnO as the primary active sites, which facilitate hydrogen-assisted CO dissociation through a mechanism distinct from formate-mediated pathways. The irradiation approach effectively addressed the instability of Zn species, a major problem in ZnO catalysis, by inhibiting defect diffusion and annihilation, and thereby maintaining CUZ site activity. Spectroscopic fingerprints of these CUZ sites could be distinguished from both SLIR and XPS Zn 3d spectra. When applied to powder catalysts, this scalable method simultaneously enhances activity, stability, and selectivity for syngas conversion. The correlation between model and powder catalytic studies provides atomic scale insights into structure–activity relationships, demonstrating that Ar-ZnO effectively simulates practical catalyst behavior. Beyond ZnO, this study introduced a promising strategy for engineering stable defect sites in oxide catalysts, offering potential applications in various processes.

METHODS

Sample Preparation and Cleaning of Ar^+-Irradiated ZnO (Ar-ZnO). ZnO(10$\bar{1}$0) surfaces (MTI Co.) were cleaned by cycles of Ar^+ sputtering (1 keV, 10 μA) at 300 K and UHV annealing at above 850 K and termed stoichiometric ZnO (S-ZnO). S-ZnO was subsequently irradiated by high fluxes of $Ar^+$with an ion energy of 1 keV and a sputtering current of 0.1 mA under normal incidence, while the surface temperature was maintained at 750 K. S-ZnO irradiated by Ar^+ for 30 , 60, and 90 min was thus termed as Ar-ZnO-30, Ar-ZnO-60, and Ar-ZnO-90, respectively. The total Ar^+ fluence applied in irradiation process was 1.8×10^{22}, 3.6×10^{22}, and 5.4×10^{22} $ions \cdot m^{-2}$, respectively. The Ar^+irradiation treatment was carried out in an

https://doi.org/10.1021/jacs.4c13234
J. Am. Chem. Soc. XXXX, XXX, XXX−XXX

UHV chamber with a base pressure of 10^{-8} mbar. During ion irradiation, the chamber was filled with argon gas at 10^{-4} mbar. Details of preparation are given in SI and Figure S22.

The experimental workflow employed separate UHV systems for high-flux ion irradiation, IRRAS, STM, and XPS measurements. Sample transfer between systems for sample preparation using Ar^+ irradiation and sample characterization inevitably resulted in atmospheric exposure. To address potential surface contamination, we implemented cleaning procedures before each series of sample characterization and reactivity measurements. Ar-ZnO surfaces were cleaned by cycles of Ar^+ sputtering (1 keV, 10 μA, 10 min) and UHV annealing at 750 K before further experiments. STM measurements after cycles of cleaning procedures did not show an obvious change of surface morphology or step edge density.

LT-STM/AFM Measurements and Image Analysis. LT-STM/AFM experiments were performed in a custom-made Createc low-temperature STM/AFM system, with a base pressure below 1×10^{-10} mbar in the STM chamber, a preparation chamber with cleaning facilities, a high-pressure (HP) cell, and a loadlock capable of accepting samples via UHV suitcase. STM images were obtained at 78 or 5 K using an electrochemically etched W tip. AFM images were obtained at 5 K using a quartz tuning fork cantilever in the qPlus design[62] with electrochemically etched Pt–Ir tip (parameters: spring constant, k = 1800 N·m^{-1}; resonance frequency, f_R = 29.4 kHz; quality factor, $Q \approx$ 150,000). The resulting 512 × 512 pixel grayscale topographic data underwent a series of processing steps using a MATLAB script (Figure S4). Initial gradient calculation enhanced edge visibility followed by the application of the Canny edge detection method to generate binary edge images. To differentiate crystallographically significant steps, a Hough transform algorithm was implemented, identifying edges aligned within 5° of the <0001> and <1$\bar{2}$10> directions and exceeding 5 pixels in length.

Quantification of step densities involved calculating total edge lengths along <0001> and <1$\bar{2}$10> directions, accounting for overlapping edges on corresponding gradient images (Figure S5). These lengths were then normalized by the image area and the corresponding Zn atom lattice spacings (0.53 nm for <0001> and 0.33 nm for <1$\bar{2}$10>) to determine site densities. The entire process is visually represented in Figures S4 and S5, showcasing the progression from raw topography to classified edge overlay. Details of step density analyses are given in SI.

In Situ AP-XPS. AP-XPS experiments were performed using a customized lab-based AP-XPS instrument (Specs GmbH.) equipped with a monochromic aluminum Kα X-ray source with spot size ~300 μm, PHOIBOS 150 HV analyzer, and infrared laser heater. The AP-XPS system contains a load-lock chamber, a preparation chamber, and an analysis chamber with base pressure <8 × 10^{-10} mbar. Before experiments, the analysis chamber was baked at 393 K for 48 h to achieve a base pressure of 7 × 10^{-10} mbar. Gas lines for CO and H_2 were baked at 393 K for 2 h and flushed several times using ultrahigh purity CO and H_2 before introducing into the chamber. The high purity CO and H_2 (YouJiaLi Co.) were further cleaned by a liquid nitrogen trap to remove H_2O and impurities before being introduced into the analysis chamber, and the CO was further cleaned by a carbonyl trap. During measurements, pass energy of the electron energy analyzer was set to 50 meV with 0.1 eV scanning steps. All AP-XPS spectra were processed using CasaXPS software, employing Shirley background subtraction and GL(30) function for peak fitting, with constrained half-peak widths for the same species. Energy calibration used the Zn 2p3/2 peak at 1021.8 eV as reference.

SLIR Measurements. IRRAS measurements of S-ZnO and Ar-ZnO were performed in a UHV apparatus combining a FTIR spectrometer (Bruker Vertex 80v) with a multichamber UHV system.[63] The measurements were performed using the IRRAS mode with a fixed incidence angle of 80°. IR spectra were recorded with a resolution of 4 cm^{-1} by using a spectrum of the clean sample as background reference. IR spectra for Ar-ZnO were processed with a 0.05 Hz low-pass filter to remove the periodic noise. The optic bench was evacuated to eliminate absorption from gas phase species (e.g., H_2O, CO, and CO_2) in the optical path. Infrared reflection absorption spectra were obtained by subtracting a background spectrum recorded before molecule exposure.

DRIFTS spectra of powder ZnO were recorded using an FTIR spectrometer (Thermo Scientific Nicolet 6700, and VERTEX 70v, Bruker) equipped with a high-temperature DRIFTS cell (Parker). Prior to reaction gas exposure, powder ZnO was alternately heated in Ar (10 mL/min), H_2/Ar mixture (10 mL/min, 5% CO/Ar), and O_2/Ar mixture flow (10 mL/min) up to 773 K in the IR cell (1 bar) and cooled down rapidly to 373 K in Ar, in order to remove surface hydroxyl groups and carbonates as much as possible.

Powder Catalyst Preparation and Characterization. Powder ZnO catalysts were prepared by coprecipitation method, as described in a previous study.[9] A specialized rotary furnace system for Argon plasma treatments (Figure S23) was used to generate surface defects on powder ZnO catalysts, designated as powder Ar-ZnO. X-ray diffraction (XRD), XPS, DRIFTS, SVUV-PIMS, and temperature-programmed surface reaction (TPSR) were used to measure the crystalline phase, valence state, the interaction of CO and CO_2 with powder ZnO, and the reactivity of powder ZnO. Details of preparation and characterization are given in the SI.

Catalytic Activity Measurements. Reactivities of CO hydrogenation on model catalysts were measured on S-ZnO, Ar-ZnO-30, Ar-ZnO-60, and Ar-ZnO-90 surfaces in a high-pressure quartz fixed bed reactor cell (HPRC), which was directly connected to a UHV system, consisting of an XPS (Thermo-Fisher ESCALAB 250Xi) chamber and an MBE chamber. XPS was used to monitor catalyst surfaces before and after the reaction. The catalytic activities of powder ZnO catalysts were measured in a fixed bed reactor. Details of catalytic activity measurements and equipment are given in SI and Figures S24 and S25.

Theoretical Calculations. DFT calculations[64,65] were performed by Vienna ab initio simulation package (VASP) with the projector augmented wave (PAW)[66,67] method. We used the generalized gradient approximation (GGA) applying Perdew–Burke–Ernzerhof (PBE) functionals.[68] The plane-wave basis set with a kinetic energy cutoff of 400 eV was specified to solve the Kohn–Sham equations. ZnO(10$\bar{1}$0) surface (Figure S26c,d) was modeled by a three double-layer slab with a (3 × 2) periodicity separated by 12 Å vacuum along Z-direction. The Monkhorst–Pack scheme for (2 × 2 × 1) k-point mesh was used to sample the Brillouin zone. The <1$\bar{2}$10>-O step was modeled by a four layer (30$\bar{3}$2) surface (Figure S26a,b) slab with a (1 × 3) periodicity separated by 12 Å vacuum along Z-direction. The Monkhorst–Pack scheme for (1 × 2 × 1) k-point mesh was used to sample the Brillouin zone. The topmost two layers of the slab and the adsorbates were relaxed with the residual forces less than 0.02 eV/Å throughout the present work without mention otherwise. GGA calculations were performed on H_2 activation on the ZnO surface because GGA and GGA+U calculations give almost the same adsorption energies and reaction barriers over the ZnO surface.[69–72] The optimized lattice constants of bulk wurtzite ZnO are $a = b$ = 3.29 Å with c = 5.30 Å, which are consistent with the previous experimental results ($a = b$ = 3.25 Å with c = 5.21 Å).[73,74]

■ ASSOCIATED CONTENT

Supporting Information

The Supporting Information is available free of charge at https://pubs.acs.org/doi/10.1021/jacs.4c13234.

Notes on the experimental method involved in the experiment, additional STM images, AP-XPS spectra, SVUV-PIMS spectra, and activity results (PDF)

■ AUTHOR INFORMATION

Corresponding Authors

Wei-Xue Li – *Hefei National Research Center for Physical Science at the Microscale, University of Science and Technology of China, Hefei 230026, China*; Email: wxli70@ustc.edu.cn

https://doi.org/10.1021/jacs.4c13234
J. Am. Chem. Soc. XXXX, XXX, XXX–XXX

Zhi Liu − *School of Physical Science and Technology, Center for Transformative Science, Shanghai Key Laboratory of High-Resolution Electron Microscopy, ShanghaiTech University, Shanghai 201210, China;* orcid.org/0000-0002-8973-6561; Email: liuzhi@shanghaitech.edu.cn

Fan Yang − *School of Physical Science and Technology, Center for Transformative Science, Shanghai Key Laboratory of High-Resolution Electron Microscopy, ShanghaiTech University, Shanghai 201210, China; State Key Laboratory of Catalysis, Dalian Institute of Chemical Physics, Chinese Academy of Sciences, Dalian 116023, China;* orcid.org/0000-0002-1406-9717; Email: fyang@shanghaitech.edu.cn

Authors

Wei-Peng Shao − *School of Physical Science and Technology, Center for Transformative Science, Shanghai Key Laboratory of High-Resolution Electron Microscopy, ShanghaiTech University, Shanghai 201210, China*

Yunjian Ling − *School of Physical Science and Technology, Center for Transformative Science, Shanghai Key Laboratory of High-Resolution Electron Microscopy, ShanghaiTech University, Shanghai 201210, China*

Hongru Peng − *School of Physical Science and Technology, Center for Transformative Science, Shanghai Key Laboratory of High-Resolution Electron Microscopy, ShanghaiTech University, Shanghai 201210, China*

Jie Luo − *Hefei National Research Center for Physical Science at the Microscale, University of Science and Technology of China, Hefei 230026, China;* orcid.org/0000-0002-0932-8331

Yunjun Cao − *State Key Laboratory of Catalysis, Dalian Institute of Chemical Physics, Chinese Academy of Sciences, Dalian 116023, China; Physical Chemistry I, Ruhr-Universität Bochum, Bochum D-44801, Germany;* orcid.org/0000-0001-8446-2242

Yihua Ran − *School of Physical Science and Technology, Center for Transformative Science, Shanghai Key Laboratory of High-Resolution Electron Microscopy, ShanghaiTech University, Shanghai 201210, China*

Jun Cai − *School of Physical Science and Technology, Center for Transformative Science, Shanghai Key Laboratory of High-Resolution Electron Microscopy, ShanghaiTech University, Shanghai 201210, China;* orcid.org/0000-0002-3806-7230

Jiayu Lv − *School of Physical Science and Technology, Center for Transformative Science, Shanghai Key Laboratory of High-Resolution Electron Microscopy, ShanghaiTech University, Shanghai 201210, China*

Bowen Zhu − *School of Physical Science and Technology, Center for Transformative Science, Shanghai Key Laboratory of High-Resolution Electron Microscopy, ShanghaiTech University, Shanghai 201210, China*

Yun Liu − *School of Physical Science and Technology, Center for Transformative Science, Shanghai Key Laboratory of High-Resolution Electron Microscopy, ShanghaiTech University, Shanghai 201210, China; Key Laboratory of Urban Pollutant Conversion and Fujian Key Laboratory of Atmospheric Ozone Pollution Prevention, Institute of Urban Environment, Chinese Academy of Sciences, Xiamen 361021, China;* orcid.org/0000-0001-9630-7610

Yuxiang Chen − *State Key Laboratory of Catalysis, Dalian Institute of Chemical Physics, Chinese Academy of Sciences, Dalian 116023, China*

Na Li − *State Key Laboratory of Catalysis, Dalian Institute of Chemical Physics, Chinese Academy of Sciences, Dalian 116023, China*

Feng Jiao − *State Key Laboratory of Catalysis, Dalian Institute of Chemical Physics, Chinese Academy of Sciences, Dalian 116023, China;* orcid.org/0000-0001-9376-7208

Huiqi Chen − *Department of Chemistry, Fudan University, Shanghai 200438, China*

Yifeng Zhu − *Department of Chemistry, Fudan University, Shanghai 200438, China*

Xin Ou − *National Key Laboratory of Materials for Integrated Circuits, Shanghai Institute of Microsystem and Information Technology, Chinese Academy of Sciences, Shanghai 200000, China;* orcid.org/0000-0002-0316-9958

Yuemin Wang − *Institute of Functional Interfaces, Karlsruhe Institute of Technology (KIT), Eggenstein-Leopoldshafen 76344, Germany;* orcid.org/0000-0002-9963-5473

Christof Wöll − *Institute of Functional Interfaces, Karlsruhe Institute of Technology (KIT), Eggenstein-Leopoldshafen 76344, Germany;* orcid.org/0000-0003-1078-3304

Qiang Fu − *State Key Laboratory of Catalysis, Dalian Institute of Chemical Physics, Chinese Academy of Sciences, Dalian 116023, China;* orcid.org/0000-0001-5316-6758

Xiulian Pan − *State Key Laboratory of Catalysis, Dalian Institute of Chemical Physics, Chinese Academy of Sciences, Dalian 116023, China;* orcid.org/0000-0002-5906-6675

Peijun Hu − *School of Physical Science and Technology, Center for Transformative Science, Shanghai Key Laboratory of High-Resolution Electron Microscopy, ShanghaiTech University, Shanghai 201210, China*

Xinhe Bao − *State Key Laboratory of Catalysis, Dalian Institute of Chemical Physics, Chinese Academy of Sciences, Dalian 116023, China;* orcid.org/0000-0001-9404-6429

Complete contact information is available at: https://pubs.acs.org/10.1021/jacs.4c13234

Author Contributions

◆W.-P.S., Y.L., H.P., J.L., and Y.C. contributed equally.

Notes

The authors declare no competing financial interest.

■ ACKNOWLEDGMENTS

This work was financially supported by the National Key R&D Program of China (2022YFA1503802), Natural Natural Science Foundation of China (M-0384, 21991152, 22303089) and Postdoctoral Science Foundation of China (2023M733373). The authors acknowledge the support from the Analytical Instrumentation Center, under contract SPST-AIC10112914, at ShanghaiTech University and Supercomputing Center of University of Science and Technology of China. The authors thank BL02B01 of Shanghai Synchrotron Radiation Facility and SPECS AP-XPS instrument supported by the National Natural Science Foundation of China, No. 11227902. The authors also thank Dr. Xiaoyi Zhan, Dr. Wugen Huang, and Dr. Hao Feng for their help and discussions during the experiment.

■ REFERENCES

(1) Campbell, C. T.; Peden, C. H. F. Oxygen vacancies and catalysis on ceria surfaces. *Science* **2005**, *309* (5735), 713−714.

(2) Diebold, U.; Li, S. C.; Schmid, M. Oxide Surface Science. *Annu. Rev. Phys. Chem.* **2010**, *61*, 129−148.

(3) Vogt, C.; Weckhuysen, B. M. The concept of active site in heterogeneous catalysis. *Nat. Rev. Chem.* **2022**, *6* (2), 89−111.
(4) Setvin, M.; Wagner, M.; Schmid, M.; Parkinson, G. S.; Diebold, U. Surface point defects on bulk oxides: atomically-resolved scanning probe microscopy. *Chem. Soc. Rev.* **2017**, *46* (7), 1772−1784.
(5) Jiao, F.; Li, J.; Pan, X.; Xiao, J.; Li, H.; Ma, H.; Wei, M.; Pan, Y.; Zhou, Z.; Li, M.; et al. Selective conversion of syngas to light olefins. *Science* **2016**, *351* (6277), 1065−1068.
(6) Pastor, E.; Sachs, M.; Selim, S.; Durrant, J. R.; Bakulin, A. A.; Walsh, A. Electronic defects in metal oxide photocatalysts. *Nat. Rev. Mater.* **2022**, *7* (7), 503−521.
(7) Wang, Y.; Wöll, C. IR spectroscopic investigations of chemical and photochemical reactions on metal oxides: bridging the materials gap. *Chem. Soc. Rev.* **2017**, *46* (7), 1875−1932.
(8) Stacchiola, D. J.; Senanayake, S. D.; Liu, P.; Rodríguez, J. A. Fundamental studies of well-defined surfaces of mixed-metal oxides: special properties of MO(x)/TiO_2(110) {M = V, Ru, Ce, or W}. *Chem. Rev.* **2013**, *113* (6), 4373−4390.
(9) Li, N.; Jiao, F.; Pan, X. L.; Ding, Y.; Feng, J. Y.; Bao, X. H. Size effects of ZnO nanoparticles in bifunctional catalysts for selective syngas conversion. *ACS Catal.* **2019**, *9* (2), 960−966.
(10) Zhang, Z.; Chen, X.; Kang, J.; Yu, Z.; Tian, J.; Gong, Z.; Jia, A.; You, R.; Qian, K.; He, S.; et al. The active sites of Cu-ZnO catalysts for water gas shift and CO hydrogenation reactions. *Nat. Commun.* **2021**, *12* (1), 4331.
(11) Jones, J.; Xiong, H.; DeLaRiva, A. T.; Peterson, E. J.; Pham, H.; Challa, S. R.; Qi, G.; Oh, S.; Wiebenga, M. H.; Pereira Hernández, X. I.; et al. Thermally stable single-atom platinum-on-ceria catalysts via atom trapping. *Science* **2016**, *353* (6295), 150−154.
(12) Shao, W.; Zhang, Y.; Zhou, Z.; Li, N.; Jiao, F.; Ling, Y.; Li, Y.; Zhou, Z.; Cao, Y.; Liu, Z.; et al. Dynamic control and quantification of active sites on ceria for CO activation and hydrogenation. *Nat. Commun.* **2024**, *15* (1), 9620.
(13) Weaver, J. F.; Hakanoglu, C.; Antony, A.; Asthagiri, A. Alkane activation on crystalline metal oxide surfaces. *Chem. Soc. Rev.* **2014**, *43* (22), 7536−7547.
(14) Liang, Z.; Li, T.; Kim, M.; Asthagiri, A.; Weaver, J. F. Low-temperature activation of methane on the IrO_2(110) surface. *Science* **2017**, *356* (6335), 299−303.
(15) Over, H. Surface Chemistry of Ruthenium Dioxide in Heterogeneous Catalysis and Electrocatalysis: From Fundamental to Applied Research. *Chem. Rev.* **2012**, *112* (6), 3356−3426.
(16) Erdem, E. Defect induced p-type conductivity in zinc oxide at high temperature: electron paramagnetic resonance spectroscopy. *Nanoscale* **2017**, *9* (31), 10983−10986.
(17) Nadupalli, S.; Repp, S.; Weber, S.; Erdem, E. About defect phenomena in ZnO nanocrystals. *Nanoscale* **2021**, *13* (20), 9160−9171.
(18) Alvarez, A.; Bansode, A.; Urakawa, A.; Bavykina, A. V.; Wezendonk, T. A.; Makkee, M.; Gascon, J.; Kapteijn, F. Challenges in the Greener Production of Formates/Formic Acid, Methanol, and DME by Heterogeneously Catalyzed CO_2 Hydrogenation Processes. *Chem. Rev.* **2017**, *117* (14), 9804−9838.
(19) Pan, X.; Jiao, F.; Miao, D.; Bao, X. Oxide-zeolite-based composite catalyst concept that enables syngas chemistry beyond Fischer−Tropsch synthesis. *Chem. Rev.* **2021**, *121* (11), 6588−6609.
(20) Kattel, S.; Ramírez, P. J.; Chen, J. G.; Rodriguez, J. A.; Liu, P. Active sites for CO_2 hydrogenation to methanol on Cu/ZnO catalysts. *Science* **2017**, *355* (6331), 1296−1299.
(21) Jiao, F.; Bai, B.; Li, G.; Pan, X.; Ye, Y.; Qu, S.; Xu, C.; Xiao, J.; Jia, Z.; Liu, W.; et al. Disentangling the activity-selectivity trade-off in catalytic conversion of syngas to light olefins. *Science* **2023**, *380* (6646), 727−730.
(22) Wöll, C. The chemistry and physics of zinc oxide surfaces. *Prog. Surf. Sci.* **2007**, *82* (2), 55−120.
(23) Han, Y. L.; Xu, J. Y.; Xie, W. B.; Wang, Z. Z.; Hu, P. Comprehensive Study of Oxygen Vacancies on the Catalytic Performance of ZnO for CO/H_2 Activation Using Machine Learning-Accelerated First-Principles Simulations. *ACS Catal.* **2023**, *13* (8), 5104−5113.
(24) Ling, Y.; Luo, J.; Ran, Y.; Liu, Z.; Li, W.-X.; Yang, F. Atomic-Scale Visualization of Heterolytic H_2 Dissociation and CO_x Hydrogenation on ZnO under Ambient Conditions. *J. Am. Chem. Soc.* **2023**, *145* (41), 22697−22707.
(25) Wang, Y. H.; Wang, G. Y.; van der Wal, L. I.; Cheng, K.; Zhang, Q. H.; de Jong, K. P.; Wang, Y. Visualizing Element Migration over Bifunctional Metal-Zeolite Catalysts and its Impact on Catalysis. *Angew. Chem., Int. Ed.* **2021**, *60* (32), 17735−17743.
(26) Geng, R.; Liu, Y.; Gao, J.; Guo, Y.; Dong, M.; Wang, S.; Fan, W.; Wang, J.; Qin, Z. The migration of Zn species on Zn/ZSM-5 catalyst during the process of ethylene aromatization. *Catal. Sci. Technol.* **2022**, *12* (13), 4201−4210.
(27) Zhao, D.; Tian, X. X.; Doronkin, D. E.; Han, S. L.; Kondratenko, V. A.; Grunwaldt, J. D.; Perechodjuk, A.; Vuong, T. H.; Rabeah, J.; Eckelt, R.; et al. In situ formation of ZnO_x species for efficient propane dehydrogenation. *Nature* **2021**, *599* (7884), 234−238.
(28) Qi, J.; Hu, X. The loss of ZnO as the support for metal catalysts by H_2 reduction. *Phys. Chem. Chem. Phys.* **2020**, *22* (7), 3953−3958.
(29) Ding, Y.; Jiao, F.; Pan, X. L.; Ji, Y.; Li, M. R.; Si, R.; Pan, Y.; Hou, G. J.; Bao, X. H. Effects of Proximity-Dependent Metal Migration on Bifunctional Composites Catalyzed Syngas to Olefins. *ACS Catal.* **2021**, *11* (15), 9729−9737.
(30) Redekop, E. A.; Cordero-Lanzac, T.; Salusso, D.; Pokle, A.; Oien-Odegaard, S.; Sunding, M. F.; Diplas, S.; Negri, C.; Borfecchia, E.; Bordiga, S.; et al. Zn redistribution and volatility in $ZnZrO_x$ catalysts for CO_2 hydrogenation. *Chem. Mater.* **2023**, *35* (24), 10434−10445.
(31) Otroshchenko, T.; Jiang, G. Y.; Kondratenko, V. A.; Rodemerck, U.; Kondratenko, E. V. Current status and perspectives in oxidative, non-oxidative and CO_2-mediated dehydrogenation of propane and isobutane over metal oxide catalysts. *Chem. Soc. Rev.* **2021**, *50* (1), 473−527.
(32) Liu, G.; Zeng, L.; Zhao, Z. J.; Tian, H.; Wu, T. F.; Gong, J. L. Platinum-Modified ZnO/Al_2O_3 for Propane Dehydrogenation: Minimized Platinum Usage and Improved Catalytic Stability. *ACS Catal.* **2016**, *6* (4), 2158−2162.
(33) Singh, A.; Hänisch, J.; Matias, V.; Ronning, F.; Mara, N.; Pohl, D.; Rellinghaus, B.; Reagor, D. Transforming insulating rutile single crystal into a fully ordered nanometer-thick transparent semiconductor. *Nanotechnology* **2010**, *21* (41), No. 415303.
(34) Rogala, M.; Klusek, Z.; Rodenbücher, C.; Waser, R.; Szot, K. Quasi-two-dimensional conducting layer on TiO_2(110) introduced by sputtering as a template for resistive switching. *Appl. Phys. Lett.* **2013**, *102* (13), 131604.
(35) Verrelli, E.; Tsoukalas, D.; Normand, P.; Kean, A. H.; Boukos, N. Forming-free resistive switching memories based on titanium-oxide nanoparticles fabricated at room temperature. *Appl. Phys. Lett.* **2013**, *102* (2), No. 022909.
(36) Ou, X.; Heinig, K. H.; Hubner, R.; Grenzer, J.; Wang, X.; Helm, M.; Fassbender, J.; Facsko, S. Faceted nanostructure arrays with extreme regularity by self-assembly of vacancies. *Nanoscale* **2015**, *7* (45), 18928−18935.
(37) Pabón, B. M.; Beltrán, J. I.; Sánchez-Santolino, G.; Palacio, I.; López-Sánchez, J.; Rubio-Zuazo, J.; Rojo, J. M.; Ferrer, P.; Mascaraque, A.; Muñoz, M. C.; et al. Formation of titanium monoxide (001) single-crystalline thin film induced by ion bombardment of titanium dioxide (110). *Nat. Commun.* **2015**, *6* (1), 6147.
(38) Keller, A.; Facsko, S. Ion-induced nanoscale ripple patterns on Si surfaces: theory and experiment. *Materials* **2010**, *3* (10), 4811−4841.
(39) Wöll, C. Structure and Chemical Properties of Oxide Nanoparticles Determined by Surface-Ligand IR Spectroscopy. *ACS Catal.* **2020**, *10* (1), 168−176.
(40) Scarano, D.; Spoto, G.; Bordiga, S.; Zecchina, A.; Lamberti, C. Lateral interactions in CO adlayers on prismatic ZnO faces: a FTIR and HRTEM study. *Surf. Sci.* **1992**, *276* (1−3), 281−298.

https://doi.org/10.1021/jacs.4c13234
J. Am. Chem. Soc. XXXX, XXX, XXX−XXX

(41) Kovácik, R.; Meyer, B.; Marx, D. F centers versus dimer vacancies on ZnO surfaces: characterization by STM and STS calculations. *Angew. Chem., Int. Ed.* **2007**, *46* (26), 4894−4897.
(42) Schröer, P.; Krüger, P.; Pollmann, J. Self-consistent electronic-structure calculations of the (10-10) surfaces of the wurtzite compounds ZnO and CdS. *Phys. Rev. B Condens. Matter* **1994**, *49* (24), 17092−17101.
(43) Cao, Y.; Luo, J.; Huang, W.; Ling, Y.; Zhu, J.; Li, W.-X.; Yang, F.; Bao, X. Probing surface defects of ZnO using formaldehyde. *J. Chem. Phys.* **2020**, *152* (7), No. 074714.
(44) Reagor, D. W.; Butko, V. Highly conductive nanolayers on strontium titanate produced by preferential ion-beam etching. *Nat. Mater.* **2005**, *4* (8), 593−596.
(45) Rodenbücher, C.; Wicklein, S.; Waser, R.; Szot, K. Insulator-to-metal transition of $SrTiO_3$: Nb single crystal surfaces induced by Ar^+ bombardment. *Appl. Phys. Lett.* **2013**, *102* (10), 101603.
(46) Myint, P.; Erb, D.; Zhang, X.; Wiegart, L.; Zhang, Y.; Fluerasu, A.; Headrick, R. L.; Facsko, S.; Ludwig, K. F. Measurement of Ehrlich-Schwoebel barrier contribution to the self-organized formation of ordered surface patterns on Ge(001). *Phys. Rev. B* **2020**, *102* (20), No. 201404.
(47) Cao, Y.; Yu, M.; Qi, S.; Wang, T.; Huang, S.; Hu, S.; Xu, M.; Yan, S. Formation and evolution of orientation-specific CO_2 chains on nonpolar ZnO(10-10) surfaces. *Sci. Rep.* **2017**, *7* (1), 43442.
(48) Noei, H.; Wöll, C.; Muhler, M.; Wang, Y. Activation of Carbon Dioxide on ZnO Nanoparticles Studied by Vibrational Spectroscopy. *J. Chem. Phys. C* **2011**, *115* (4), 908−914.
(49) Weilach, C.; Spiel, C.; Föttinger, K.; Rupprechter, G. Carbonate formation on Al_2O_3 thin film model catalyst supports. *Surf. Sci.* **2011**, *605* (15−16), 1503−1509.
(50) Buchholz, M.; Weidler, P.; Bebensee, F.; Nefedov, A.; Wöll, C. Carbon dioxide adsorption on a ZnO(10-10) substrate studied by infrared reflection absorption spectroscopy. *Phys. Chem. Chem. Phys.* **2014**, *16*, 1672−1678.
(51) Wang, Y.; Kovácik, R.; Meyer, B.; Kotsis, K.; Stodt, D.; Staemmler, V.; Qiu, H.; Traeger, F.; Langenberg, D.; Muhler, M.; et al. CO_2 activation by ZnO through the formation of an unusual tridentate surface carbonate. *Angew. Chem., Int. Ed.* **2007**, *46* (29), 5624−5627.
(52) Hussain, G.; Sheppard, N. The generation of formate species on the surface of zinc oxide near 200°C from CO with H_2, or from CO alone, as shown by infrared spectroscopy. *Spectrochim. Acta, Part A* **1987**, *43* (12), 1631−1637.
(53) Ling, Y. J.; Luo, J.; Ran, Y. H.; Cao, Y. J.; Huang, W. G.; Cai, J.; Liu, Z.; Li, W. X.; Yang, F.; Bao, X. H. Dynamic chemical processes on ZnO surfaces tuned by physisorption under ambient conditions. *J. Energy Chem.* **2022**, *72*, 258−264.
(54) Lai, Z. Z.; Sun, N. L.; Jin, J. M.; Chen, J. F.; Wang, H. F.; Hu, P. Resolving the Intricate Mechanism and Selectivity of Syngas Conversion on Reduced $ZnCr_2O_x$: A Quantitative Study from DFT and Microkinetic Simulations. *ACS Catal.* **2021**, *11* (21), 12977−12988.
(55) Frankcombe, T. J.; Liu, Y. Interpretation of oxygen 1s X-ray photoelectron spectroscopy of ZnO. *Chem. Mater.* **2023**, *35* (14), 5468−5474.
(56) Liu, Q.; Han, Y.; Cao, Y.; Li, X.; Huang, W.; Yu, Y.; Yang, F.; Bao, X.; Li, Y.; Liu, Z. In-situ APXPS and STM study of the activation of H_2 on ZnO(10−10) surface. *Acta Phys. -Chim. Sin.* **2018**, *34* (12), 1366−1372.
(57) Li, J.; Nolan, M.; Detavernier, C. A step toward correct interpretation of XPS results in metal oxides: A case study aided by first-principles method in ZnO. *J. Chem. Phys.* **2023**, *159* (3), No. 034702.
(58) Amann, P.; Klötzer, B.; Degerman, D.; Köpfle, N.; Götsch, T.; Lömker, P.; Rameshan, C.; Ploner, K.; Bikaljevic, D.; Wang, H.-Y.; et al. The state of zinc in methanol synthesis over a Zn/ZnO/Cu(211) model catalyst. *Science* **2022**, *376* (6593), 603−608.
(59) Kurtz, M.; Strunk, J.; Hinrichsen, O.; Muhler, M.; Fink, K.; Meyer, B.; Wöll, C. Active sites on oxide surfaces: ZnO-catalyzed synthesis of methanol from CO and H_2. *Angew. Chem., Int. Ed.* **2005**, *44* (18), 2790−2794.
(60) Wilmer, H.; Kurtz, M.; Klementiev, K. V.; Tkachenko, O. P.; Grünert, W.; Hinrichsen, O.; Birkner, A.; Rabe, S.; Merz, K.; Driess, M.; et al. Methanol synthesis over ZnO: A structure-sensitive reaction? *Phys. Chem. Chem. Phys.* **2003**, *5* (20), 4736−4742.
(61) Strunk, J.; Kähler, K.; Xia, X.; Muhler, M. The surface chemistry of ZnO nanoparticles applied as heterogeneous catalysts in methanol synthesis. *Surf. Sci.* **2009**, *603* (10), 1776−1783.
(62) Giessibl, F. J. High-speed force sensor for force microscopy and profilometry utilizing a quartz tuning fork. *Appl. Phys. Lett.* **1998**, *73* (26), 3956−3958.
(63) Heilmann, R.; Kolodziejczak, J.; Bruccoleri, A.; Gaskin, J.; Schattenburg, M. Demonstration of resolving power $\lambda/\Delta\lambda$ > 10,000 for a space-based x-ray transmission grating spectrometer. *Appl. Opt.* **2019**, *58*, 1223.
(64) Kresse, G.; Furthmuller, J. Efficiency of ab-initio total energy calculations for metals and semiconductors using a plane-wave basis set. *Comput. Mater. Sci.* **1996**, *6* (1), 15−50.
(65) Kresse, G.; Furthmüller, J. Efficient iterative schemes for ab initio total-energy calculations using a plane-wave basis set. *Phys. Rev. B* **1996**, *54* (16), 11169−11186.
(66) Blöchl, P. E. Projector augmented-wave method. *Phys. Rev. B* **1994**, *50* (24), 17953−17979.
(67) Kresse, G.; Joubert, D. From ultrasoft pseudopotentials to the projector augmented-wave method. *Phys. Rev. B* **1999**, *59* (3), 1758−1775.
(68) Perdew, J. P.; Burke, K.; Ernzerhof, M. Generalized gradient approximation made simple. *Phys. Rev. Lett.* **1996**, *77* (18), 3865.
(69) Meyer, B.; Rabaa, H.; Marx, D. Water adsorption on ZnO(10-10): from single molecules to partially dissociated monolayers. *Phys. Chem. Chem. Phys.* **2006**, *8* (13), 1513−1520.
(70) Pala, R. G. S.; Metiu, H. Selective promotion of different modes of methanol adsorption via the cation substitutional doping of a ZnO(10-10) surface. *J. Catal.* **2008**, *254* (2), 325−331.
(71) Gu, X. K.; Huang, C. Q.; Li, W. X. First-principles study of single transition metal atoms on ZnO for the water gas shift reaction. *Catal. Sci. Technol.* **2017**, *7* (19), 4294−4301.
(72) Gu, X. K.; Qiao, B. T.; Huang, C. Q.; Ding, W. C.; Sun, K. J.; Zhan, E. S.; Zhang, T.; Liu, J. Y.; Li, W. X. Supported Single Pt_1/Au_1 Atoms for Methanol Steam Reforming. *ACS Catal.* **2014**, *4* (11), 3886−3890.
(73) Escudero, R.; Escamilla, R. Ferromagnetic behavior of high-purity ZnO nanoparticles. *Solid State Commun.* **2011**, *151* (2), 97−101.
(74) Abrahams, S. C.; Bernstein, J. Remeasurement of the structure of hexagonal ZnO. *Acta Cryst. B* **1969**, *25*, 1233−1236.

https://doi.org/10.1021/jacs.4c13234
J. Am. Chem. Soc. XXXX, XXX, XXX−XXX